



**Universidad de los Andes**

PHYSICS DEPARTMENT

MEASUREMENT AND CHARACTERIZATION OF  
GRANULATION PATTERN IN THE IAG SOLAR FLUX  
SPECTRUM

*BSc Physics Final Project*

**Author:**

Claudia Alejandra Cuellar Nieto

**Advisor:**

Benjamin Oostra Vannoppen

Nov 2025

## **Abstract**

Hello, this is my work :D

## **Acknowledgements**

Thanks :b

# Contents

<b>List of Figures</b>	<b>3</b>
<b>1 Introduction: The Sun's granulation pattern</b>	<b>5</b>
1.1 Convective motion . . . . .	6
1.2 Solar granulation pattern . . . . .	6
1.2.1 The three signatures of convection . . . . .	7
1.3 IAG Solar Flux Atlas . . . . .	7
1.4 IAG Spatially Resolved Quiet Sun Atlas . . . . .	8
1.5 Motivation . . . . .	8
<b>2 Literature Review: Convective movement in the Sun</b>	<b>10</b>
2.1 The solar interior and the solar outer atmosphere . . . . .	10
2.2 The solar convection Zone . . . . .	13
2.2.1 The convection movement in the sun . . . . .	13
2.2.2 Dynamics of solar convection . . . . .	13
2.2.3 The Schwarzschild condition . . . . .	15
2.3 The Solar Photosphere . . . . .	16
2.3.1 Static photosphere: Limb darkening phenomenon . . . . .	16
2.3.2 Dynamic photosphere: The C-curved profile bisector. . . . .	18
2.4 The three signature of convection . . . . .	19
2.4.1 Line broadening . . . . .	19
2.4.2 Line profile bisector asymmetry . . . . .	20

2.4.3	Line depth-dependent wavelength shifts . . . . .	21
2.4.4	Solar granulation pattern . . . . .	21
2.4.5	Chromodependence characterization . . . . .	22
<b>3</b>	<b>Methodology: The blend-free list of Fe I lines</b>	<b>25</b>
3.1	Computational approach . . . . .	25
3.2	Blend-free Fe I line list . . . . .	26
3.2.1	Selection method for Fe I lines . . . . .	26
3.2.2	Observational requirement . . . . .	27
<b>4</b>	<b>Results and discussion: Granulation pattern and Characterization of chromodependence</b>	<b>28</b>
4.1	The first signature . . . . .	28
4.1.1	Detailed view of line broadening . . . . .	28
4.2	The second signature . . . . .	30
4.2.1	Detailed view of line profile bisector asymmetry . . . . .	30
4.3	The third signature . . . . .	31
4.3.1	Chromodependence on the granulation pattern . . . . .	31
4.3.2	Characterization of chromodependence on granulation pattern . . . . .	32
4.3.3	Frequency shifts for rotation hypothesis . . . . .	34
4.4	Higher quality graphs . . . . .	37
<b>5</b>	<b>Conclusions</b>	<b>39</b>
<b>A</b>	<b>Z-score Standardization</b>	<b>40</b>
<b>B</b>	<b>The third derivate relation</b>	<b>42</b>
<b>C</b>	<b>Visualizer for outliers</b>	<b>43</b>

# List of Figures

2.1	The general structure of the Sun. Image modified from [1]. . . . .	11
2.2	The first clear photography of the photosphere where is visible the granulation pattern. Image taken from [2] . . . . .	12
2.3	Diagram for the parcel of material displaced so slowly that remains in horizontal pressure. Image taken from [1] . . . . .	15
2.4	A view of granulation on the Sun's surface. The central regions exhibit blueshifts while the edges display redshifts. Image taken from [3] . . . . .	16
2.5	Squared profile for the disk intensity at increasing wavelengths. Image taken from [4] . . . . .	17
2.6	A time sequence showing granule evolution where the time intervals are about a minute. Image taken from [4] . . . . .	18
2.7	The C-curved profile bisector. In the infrared shown to be less pronounced than violet range. . . . .	19
2.8	Asymmetries on an average absorption line. Can be observed the differences in intensity redshift profile. Image taken from [5] . . . . .	20
2.9	Granulation pattern for the IAG spatially resolved quiet sun atlas, is shown to have a strong chromodependence in the weaker lines. Image taken from [6]. . .	22
2.10	Contributions on angular momentum. Image taken from [4]. . . . .	23
4.1	Line core curvature in the Solar Flux Atlas. Is visible a characteristic curve with line depth-dependence along wavelength. . . . .	29

4.2	Line core curvature in the Solar Flux Atlas. The near infrared range presents a natural division due telluric lines in the atmosphere. . . . .	30
4.3	Line profile bisector slope for the Solar Flux Atlas separated by wavelength range. The behavior of the plot is according to the C-curved shape of the line bisector affected by convection movement. . . . .	31
4.4	Granulation pattern obtained for the Solar Flux Atlas. The wavelength shift dependence is along the line depth. . . . .	32
4.5	Granulation pattern for the Solar Flux Atlas with color curves. The tendency on the curves is more pronounced in the violet and red range. . . . .	33
4.6	Coefficient tendency for the second order polynomial fit in each color curve. All of the coefficients show a rational increment with decreasing wavelength. . . . .	33
4.7	Comparision between atlases with velocity bins for the relation between wavelength and line depth. For each velocity bin was plotted wavelength against line depth to measure a frequency shift with a first order polynomial fit. . . . .	35
4.8	Comparision between atlases with velocity bins for the relation between wavelength and line depth. The first order fit is showed for each velocity bin. . . . .	36
4.9	We realized the same graphic for the comparision with the Ellwarth article to show the less scattered points. . . . .	38

# Chapter 1

## Introduction: The Sun's granulation pattern

For decades, the solar spectrum has served as the fundamental reference point for spectroscopic analysis and characterization. As our nearest star, the Sun has enabled comprehensive studies of stellar composition. However, advances in optical instrumentation have recently revealed previously undetected spectral details, providing new insights into even the most basic solar properties from dynamics to surface geometry. One of this advances is the granulation pattern due to convection motion, which is revealed by three fundamental signatures of its hydrodynamics: Line broadening, line profile bisector asymmetry, and line-depth dependence of the convective blueshift.

Inspired by Gray's foundational research [7], this project seeks to extract the granulation pattern from the IAG Solar Flux Atlas to calculate relative velocities and perform detailed analysis. A parallel focus will investigate the line depth-dependence wavelength shifts detected in absorption line profiles (the third signature of convection), which currently obscures the universality of the pattern.

## 1.1 Convective motion

The stellar spectrum serves as astronomy's primary source of information, particularly regarding a star's composition and relative velocity. However, convective motions in the stellar photosphere complicate spectral interpretation by inducing differential velocities in individual spectral lines. Specifically, fluid movements caused by density variations from temperature fluctuations in the Sun's outermost layer modify the spectrum, causing each spectral line to display distinct relative velocities as we can relate to different research (see [8, 7, 9, 6] and references there in). Persistent convective motion generates a granular structure in solar photospheric images. One of the first people to discover the pattern was Janssen in 1885, who detected a granulation movement in the photosphere. Lately, in 1901 Plasketts associated this pattern with the same of convective cells in Bernard's experiment [4]. Where fluids heated from below represent hot rising gas elements convecting heat to the surface. This characteristic configuration gives the name *granulation* to all observable signs of the convection.

## 1.2 Solar granulation pattern

A plot of Doppler shift against line depth is called *Granulation Pattern*; it shows that weaker lines are more blueshifted. When the Sun pushes material up through its outer layer, the spectrum exhibits a blueshift. As this material subsequently cools and falls back through the atmosphere, it produces a redshift, but emits less light, making the blueshift dominant. This phenomenon has been particularly documented by David Gray, whose work has significantly improved the precision of stellar radial velocity measurements. This improvement stems primarily from Gray's observation that granulation patterns in stars resemble solar patterns, differing only by a scaling factor. These findings are particularly significant given the considerable challenges in obtaining such parameters for other stars, which are affected by spectral noise, stellar proper motions, and relative velocity uncertainties [7]. Furthermore, analysis of solar granulation patterns contributes to the understanding and validation of photospheric hydrodynamic models [10]. Such analysis enables improved calibration when testing dynamic atmospheric models.

### 1.2.1 The three signatures of convection

Due to convection motion, there's three distinct granulation signatures that can be identified in stellar spectra: Line broadening, line profile bisector asymmetry, and line-depth dependent shifts in absorption lines [11]. The third signature exhibits a correlation between line depth and wavelength shift [7], for which neutral iron lines (Fe I) serve as optimal calibration references due to their high abundance, minimal thermal broadening and limited isotopic variation. This approach offers the additional advantage of deriving natural wavelengths from a single source, thereby eliminating potential discrepancies.

On the way of treating the Sun as any other star, which does not have the proximity for spectra study, we search for obtain the most accurate and precise granulation pattern. Which is possible if we take the most accurate and precise solar atlas.

## 1.3 IAG Solar Flux Atlas

In 2016, Reiners et al. [9] published the unprecedented precision *Institut für Astrophysik Göttingen (IAG)* Solar Flux Atlas obtained with the FTS *Fourier Transform Spectrograph*, simultaneously reporting convective blueshifts for a sample of neutral iron lines. This atlas provides highly precise and accurate data, with radial velocity uncertainties on the order of  $\pm 10 m/s$  across the wavelength range of 4050 to 10650 Å. In contrast to other FTS atlases, the entire visible wavelength range was observed simultaneously using only one spectrograph setting[9]. In 2016, the resulting granulation pattern appeared notably scattered and noisy, attributable to the rudimentary line position measurement methodology employed, and the poorly curated line selection, which included numerous blended features, outdated wavelength references and incomplete spectral coverage. The exceptional quality of the IAG spectrum enables more accurate determination of convective blue-shifts when analyzed through refined methods.

## 1.4 IAG Spatially Resolved Quiet Sun Atlas

In 2023, Ellwarth et al.[6] observed and published the *Institut für Astrophysik Göttingen (IAG) Spatially Resolved Quiet Sun Atlas* obtained with the FTS *Fourier Transform Spectrograph*. This atlas has the advantage of using observations from the disc center ( $\mu = 1.0$ ) towards the solar limb ( $\mu = 0$ ), where  $\mu = \cos(\theta)$ . The research had the objective of studying the blueshift exhibits variations from the disc centre to the solar limb due to differing projection angles onto the solar atmosphere.

Our principal objective is to establish a characterization of the granulation pattern by treating the Sun as any other star. This approach allows us to develop methods that can be directly scaled and applied to other solar-type stars. However, to accurately analyze relative velocities and dynamics, we must account for insights that can only be corrected using the Spatially Resolved Quiet Sun Atlas.

## 1.5 Motivation

During the first semester of 2025, physics student at the Universidad de los Andes Manuel Fuentes implemented these improvements in his computational project, focusing specifically on the visible spectral range  $4050 - 10650 \text{ \AA}$ . By developing enhanced measurement techniques and employing a carefully curated line list that fully covers the IAG-VIS range with updated wavelength references [12], Fuentes achieved significantly sharper granulation patterns compared to previous analyses. This optimized approach demonstrates how proper line selection and modern wavelength standards can extract more reliable convective signatures from high-quality solar spectra.

With guidance of professor Benjamin, the measurement of granulation patterns taking into account the near infrared range was realized. This region contains spectral lines originating from deeper layers of the solar photosphere, which are consequently weaker. Furthermore, these lines represent a rich source of valuable information [13], though they require adapting the measurement methodology. Then, characterization of solar dynamics and line asymmetries based on granulation pattern observations was started.

By addressing these challenges, the objectives for this project were to produce a robust characterization of the solar granulation pattern and insights into the photosphere's geometry. These efforts were guided by the central research question: What are the direct consequences of solar dynamics on its spectrum?

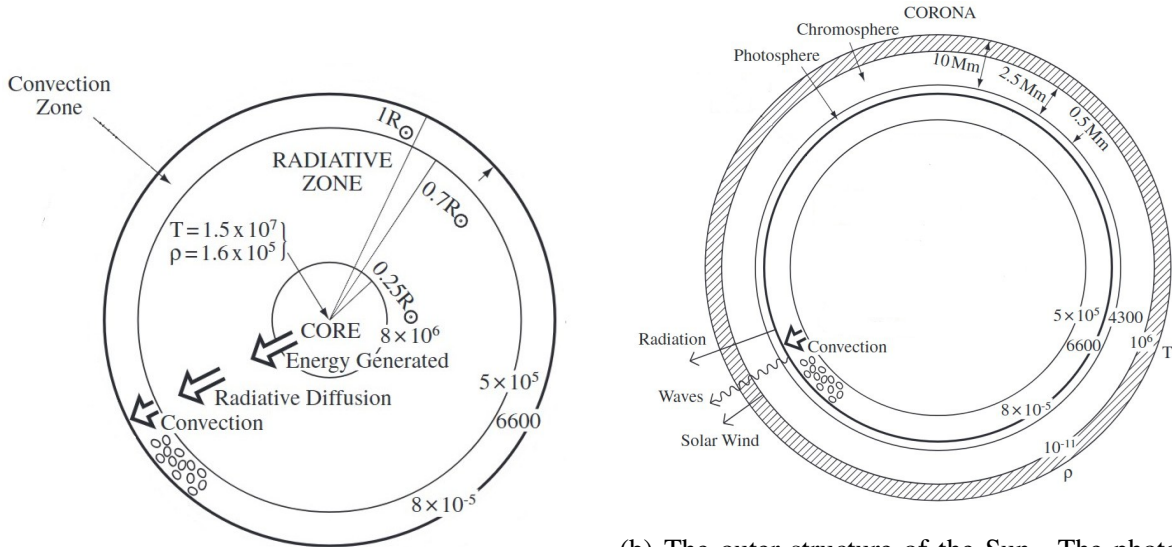
# **Chapter 2**

## **Literature Review: Convective movement in the Sun**

As previously mentioned, David Gray [7, 11, 14] has significantly advanced the study of granulation patterns in the solar photosphere, with a particular focus on measuring their associated relative velocities with high precision. These developments have enabled more accurate characterizations of other stars by extrapolating the physical principles observed in the Sun. This chapter explores the three signatures of convective motion in the Sun photosphere, and how this reveal the hydrodynamic on this outermost layer. Furthermore, is given the point of view of different authors respect the reasons behind the chromodependence on the granulation patterns.

### **2.1 The solar interior and the solar outer atmosphere**

The Sun is classified as a yellow dwarf star of spectral type G2V, title achieved for a big amount of hot hydrogen (ionised H in 90 percent) and helium (in 10 percent). What makes this star really unique is his proximity to earth and the facility to study from the planet with precision. In general, the Sun is divided in two fundamental parts: The solar interior and the solar outer atmosphere.



(a) The interior structure of the Sun. The convection zone is the responsible by the general movement that characterize the third signature.

(b) The outer structure of the Sun. The photosphere is the layer of the sun where is visible the convection cells overshooting from the convection zone.

Figure 2.1: The general structure of the Sun. Image modified from [1].

As shown in the figure 2.1a the overall structure of the solar interior is core, radiative and convective zone. Across then the density and temperature falls significantly, as the energy is slowly transferred outwards by radiative diffusion. Some models of the interior structure give a core temperature of  $1.6 \times 10^7 K$  and density to  $1.6 \times 10^5 \text{ kg/m}^3$ , high enough for thermonuclear reactions and remains the central material in plasma like a gigantic atomic reactor. This characteristic allow the collisions, absorptions and reemisions of photons that made this zone opaque. In consequence, there exists an increase of the wavelength from high-energy gamma rays to visible light.

On the other hand, the figure 2.1b show the overall structure of the solar outer atmosphere which consist in photosphere, chromosphere and corona. In this part the density decreases rather rapidly with height above solar surface, and the temperature decrease to  $4300 K$  for then rises through the transition region. Thereafter, the temperature falls slowly expanding outwards as the solar wind. The most relevant layer is the photosphere, a thin layer of plasma that emits most of the solar radiation and emits a continuous spectrum with superimposed dark absorption

lines. Most of this wavelengths are absorbed by the chromosphere, which is transparent[1]. From this the photosphere emits a continuous spectrum with superimposed dark absorption lines where most of this wavelengths are absorbed by the chromosphere [1]. The target layers of this study are the convection zone and the photosphere, which will focus in further sections.

For this research, the two target layers of the Sun are the convection zone and the photosphere.

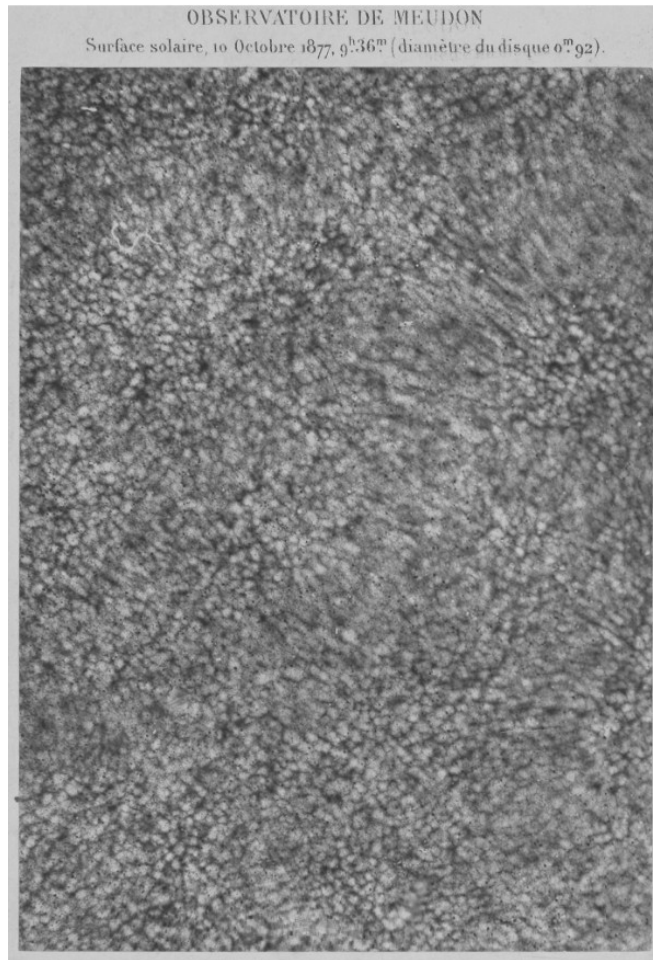


Figure 2.2: The first clear photography of the photosphere where is visible the granulation pattern. Image taken from [2]

As we shown in the figure 2.2, in 1877 Janssen took the first clear photography of the granules in the photosphere [2]. This was the starting point for different studies across the pattern of granules. In 1930 Unsold pointed out that the layers below the photosphere should be con-

vective unstable [4]. Later, Plasketts relationed these granules with the Bernard's laboratory measurements of fluids convection. This statement are based on fluids heated from below representing hot rising gas elements convecting heat to surface [15]. This hot rising gas elements are known as granulation, and each individual region—spanning approximately 700 km in size and lasting between five to ten minutes—is referred to as a granule. The understanding of photospheric granules as convective cells leads the thought to the existence of a zone responsible of the convective motion.

## 2.2 The solar convection Zone

Starting at the  $0.86R_{\odot}$  lies the zone where the dynamics processes took place, the great temperature gradient across the layer allow the process of convection [1].

### 2.2.1 The convection movement in the sun

As we mentioned, the convective movement are based on fluids heated from below representing hot rising gas granules or *convective cells* convecting heat to the photosphere [15]. In this case, solar convection occurs in a highly compressible, stratified gas which leads to determine the conditions under which we expect convection and the dynamics of the granules [4].

### 2.2.2 Dynamics of solar convection

From the core, He nuclei is built from H nuclei in the proton-proton cycle as say equation (2.1).



Where from the H nuclei is liberated an considerable amount of high frecuency  $\gamma$ -rays ( $26.7\text{MeV}$ ) and the energy of two neutrinos ( $0.5\text{MeV}$ ). However, the strong Coulumb repulsion between positivly charged nuclei increases as the product of their nuclear charges, so only lightest elements will have appreciable reaction probabilities. As the electrons recombine with others particles the photons can be absorbed more easily. With this, decrease the radiative conductivity

and increases the temperature gradient with the opacity [4]. The decrease of temperature allow a convective instability and beyond a convective turbulence. When reaches the low photosphere, some radiation scape from the sun and the material returns to the convective stability [1].

This inclines to stablish an onset of convection: If  $T$  is increased to a value  $T'$ , the granule will expand rapidly to achieve a new pressure equilibrium with its surroundings. Where is suppose the granules as vertical stratified plasma in hydrostatic equilibrium with pressure ( $P(r)$ ); density ( $\rho(r)$ ); and temperature ( $T(r)$ ), the same as its surroundings at radial distance  $r$  from the center of the star.

The lower-density gas experiences a bouyancy force, which will cause it to rise. The bouyancy force will disappear when the density has dropped to the same value as the new surroundings, after an element has traveled a distance  $l$ . Let be  $T'_n$  the new temperature and that of its surroundings  $T_n$ , the adiabatic and radiative gradient for the element follows the equation (2.2).

$$T_n = T + \left( \frac{dT}{dr} \right)_R l \quad | \quad T'_n = T' + \left( \frac{dT}{dr} \right)_{ad} l \quad (2.2)$$

Where  $ad$  references for adiabatic gradient;  $R$  is for radiative gradients; and taking  $l$  small. Since we have assumed radiative equilibrium, the  $R$  denotes the gradient present in the stellar atmosphere. Two conditions can arise from here (see equation (2.3)): The radiative gradient is unstable, so convection pattern is stablish and viceversa.

$$-\left( \frac{dT}{dr} \right)_R > \left( \frac{dT}{dr} \right)_{ad} \quad (2.3)$$

If the convection pattern is stablish, the element continues to expand further and rise. Otherwise, the element begins to contract, becomes heavier, and begins to move down to its original position.

This onset of instability when the vertical temperature gradient is too large is explained by the Schwarzschild condition.

### 2.2.3 The Schwarzschild condition

Taking the element described before, now suppose an elementary parcel of material displaced so slowly that remains in horizontal pressure equilibrium (see figure 2.3).

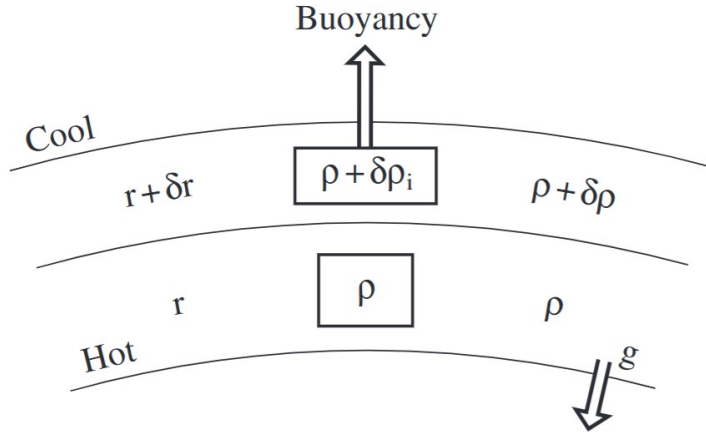


Figure 2.3: Diagram for the parcel of material displaced so slowly that remains in horizontal pressure. Image taken from [1]

If the motion is adiabatic there is no heat exchange with surroundings, the ratio between the density and pressure is constant. This generates a criterion for the presence of convection known as the Schwarzschild condition (2.4).

$$-\frac{dT}{dr} > \frac{\gamma - 1}{\gamma} \left( \frac{GM_{\odot}m}{r^2 k_B} \right) \quad (2.4)$$

Where  $k_B$  refers to Boltzmann constant;  $G$  the gravitational constant;  $M_{\odot}$  the solar mass;  $m$  the mass of the granule; and  $\gamma$  the degree freedom of the fluid. As the presence of convection reduces the temperature gradient from the higher value it would have assumed under radiative transport alone to the essentially adiabatic value [4].

All of the material and energy generated by convection ended up to low photosphere, where the granules shows different properties examined in after sections.

## 2.3 The Solar Photosphere

Since 1874, when Langley gives a detailed description of granulation on the photosphere, the astronomers have been studied different motions and reactions on the outermost solar layer [1]. The distinct pattern of granules with dynamic behavior becomes apparent, where individual areas continuously emerge and disappear (see figure 2.4).

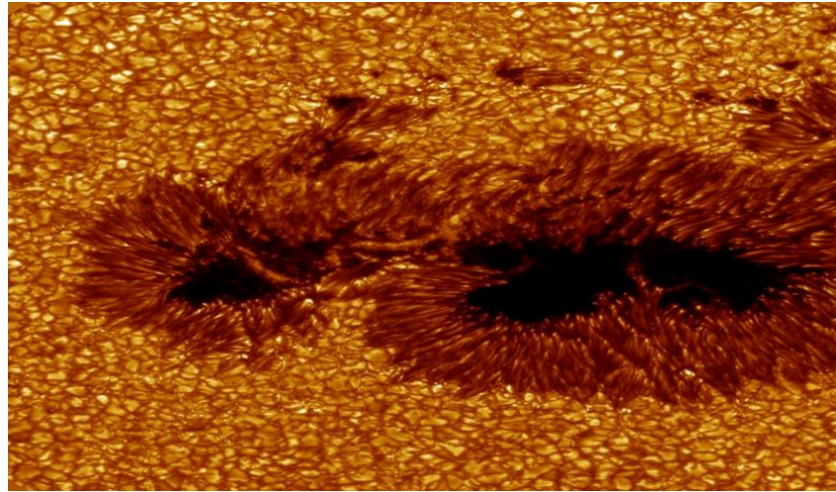


Figure 2.4: A view of granulation on the Sun’s surface. The central regions exhibit blueshifts while the edges display redshifts. Image taken from [3]

The bright areas of granules correspond to regions where hot gas rises through the solar atmosphere. As this gas releases energy in the form of photons at the photosphere, it cools and subsequently descends, creating the darker regions of granules [16, 10].

### 2.3.1 Static photosphere: Limb darkening phenomenon

Cause the temperature decrease from the higher layers, the photosphere intensity falls off towards the solar limb. Consequently, the disk intensity profile becomes more squared at increasing wavelength (see figure 2.5).

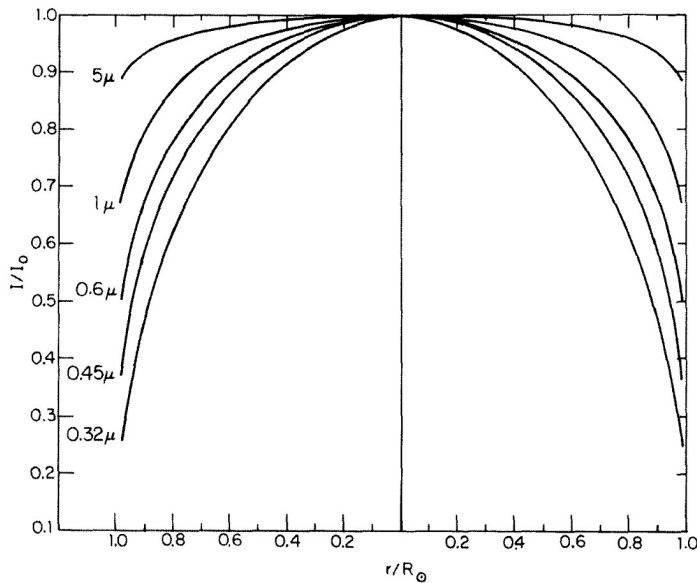


Figure 2.5: Squared profile for the disk intensity at increasing wavelengths. Image taken from [4]

This effect is known as *Limb darkening phenomenon*. The analysis of this effect provides a direct technique for determining the photosphere temperature structure along depth. Furthermore, these granules has shown to be in continual motion (see figure 2.6).

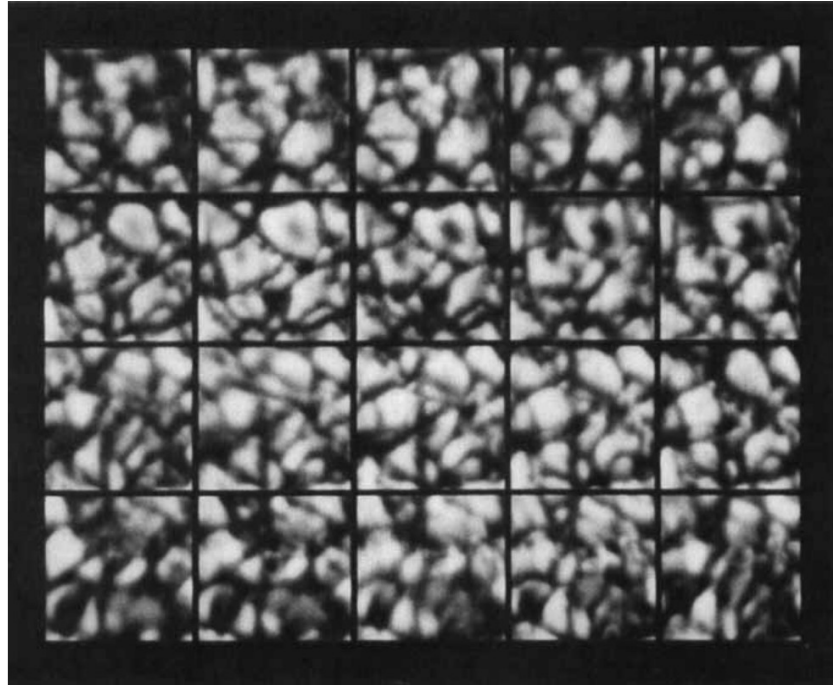


Figure 2.6: A time sequence showing granule evolution where the time intervals are about a minute. Image taken from [4]

This perpetual motion across the layer generates asymmetries on the absorption lines.

### 2.3.2 Dynamic photosphere: The C-curved profile bisector.

Observing the dynamic of the granules, there appear a height dependence of the granular velocities: The velocity of an upward moving granule decays much less rapidly than its excess brightness. Changes in the granulation structure, contrast and velocity field around the spots and network have been inferred indirectly from observations of Fraunhofer line profile shapes [4]. The result is characteristically C-Curved profile bisector (see figure 2.7).

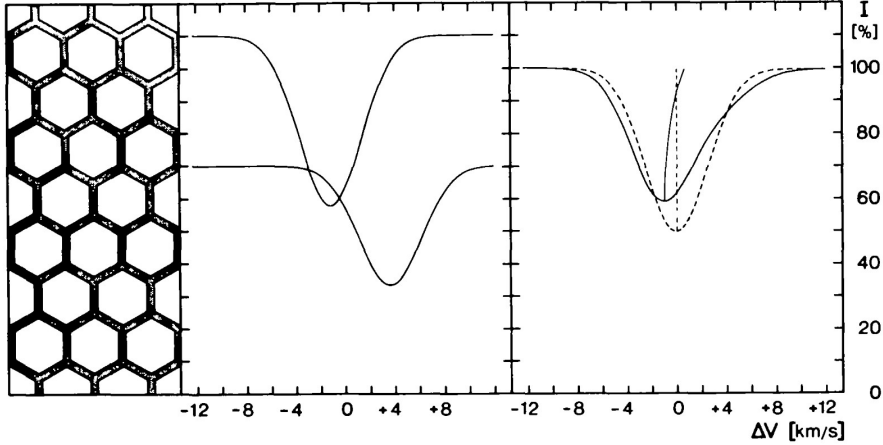


Figure 2.7: The C-curved profile bisector. In the infrared shown to be less pronounced than violet range.

The process of the creation in this c-curved profile bisector is divided in three stages. First, the line profile near its mid-depth portion is formed in the most rapidly upflowing bright material (Blueshifted). Then, the deepest portion of the line core is formed higher in the decelerated upflow (Less Blueshifted). Finally, the line wings where the opacity is least, tend to be formed deepest in the cool (Redshifted).

This dynamic process induces perturbations in spectral absorption lines, line profile asymmetries, and line depth-dependent wavelength shifts [11] known as the three signatures of convection.

## 2.4 The three signature of convection

The signatures of convection in stars are described by Gray in his research [7, 14, 11] about the principal characteristics in the spectra to identify and treat the asymmetries due to convective motion.

### 2.4.1 Line broadening

Due to the limb darkening phenomenon and atmospheric absorption, there exists two types of line cores: Strongest and weaker lines [11]. Where strongest refers to more curved than

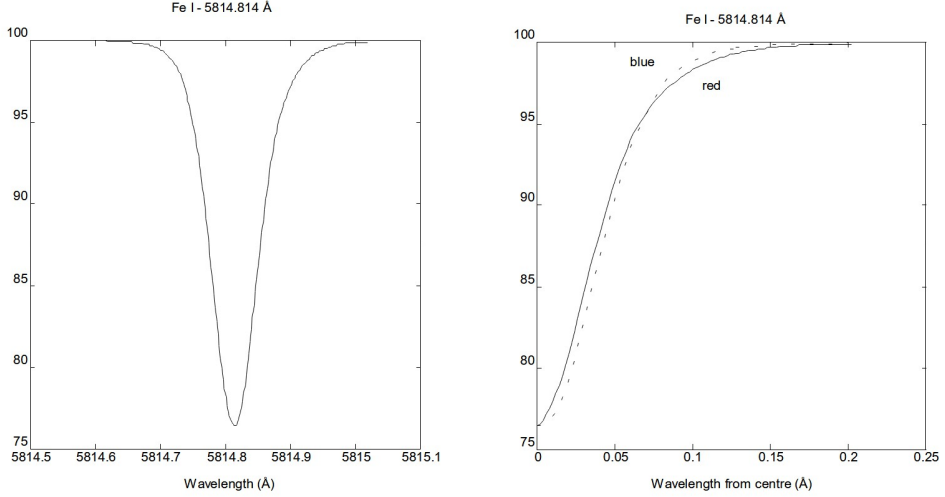


Figure 2.8: Asymmetries on an average absorption line. Can be observed the differences in intensity redshift profile. Image taken from [5]

weaker lines. This effect is measurable with the second derivate in the observed wavelength, that representing the core curvature (see equation (2.5)).

$$C_c = \lambda^2 \left( \frac{d^2 p(\lambda)}{d\lambda^2} \right) \quad (2.5)$$

Where  $p(\lambda)$  is the polynomial fit for the core evaluated on the observed wavelength. In the near infrared range we can denote a natural bands or groups of lines which are separated for the teluric elements, on others words, elements like oxygen and CO<sub>2</sub> that are absorbed by the atmosphere. This range are invisible for the spectra, and it helps us to detect the natural bands in the near infrared curvature profile.

#### 2.4.2 Line profile bisector asymmetry

As demonstrated by Nieminen [5], the asymmetry occurs because the c-curved profile bisector reflects velocity variations and a bisector slope (see figure 2.8).

According to Kirchhoff's laws, absorption line formation requires lower temperature conditions, which are found precisely in the Sun's outermost atmospheric layers [16]. These regions not only provide the appropriate temperatures for absorption line formation but also exhibit

comparatively higher opacity. Among all available spectral lines, those from neutral iron (Fe I) are particularly valuable for solar granulation studies due to two key characteristics: they display significant opacity and relatively low thermal broadening. These properties make Fe I lines excellent tracers of granulation patterns in the solar photosphere [5].

These asymmetries can be measured using the third derivate relation for the line bisector (see equation (2.6)).

$$\frac{c}{\lambda} \left( \frac{1}{3C_c^2} \right) \left( \frac{d^3 p(\lambda)}{d\lambda^3} \right) \quad (2.6)$$

Where  $C_c$  refers to the core curvature in the equation (2.5).

### 2.4.3 Line depth-dependent wavelength shifts

Many studies across the years have detected and observed the phenomena of wavelength shifts against the line depth, or as it is called, chromodependence in the granulation pattern. This behavior was showed to be more present in the weaker lines which are related to infrared and violet range.

### 2.4.4 Solar granulation pattern

The solar granulation pattern is a plot of relative velocity against line depth, as shown in the figure 2.9.

The importance of this pattern lies in stars resemble solar patterns, differing only by a scaling factor (see [11]). Furthermore, these analysis contributes to the understanding and radiation of photospheric hydrodynamic models [10, 7]. However, for the measurement is necessary the understanding of the convective blueshift.

#### Convective Blueshift

When the Sun pushes material up through its outer layer, the spectrum exhibits a blueshift. As this material subsequently cools and falls back through the atmosphere, it produces a redshift, but emits less light, making the blueshift dominant. That can be measure by the Doppler

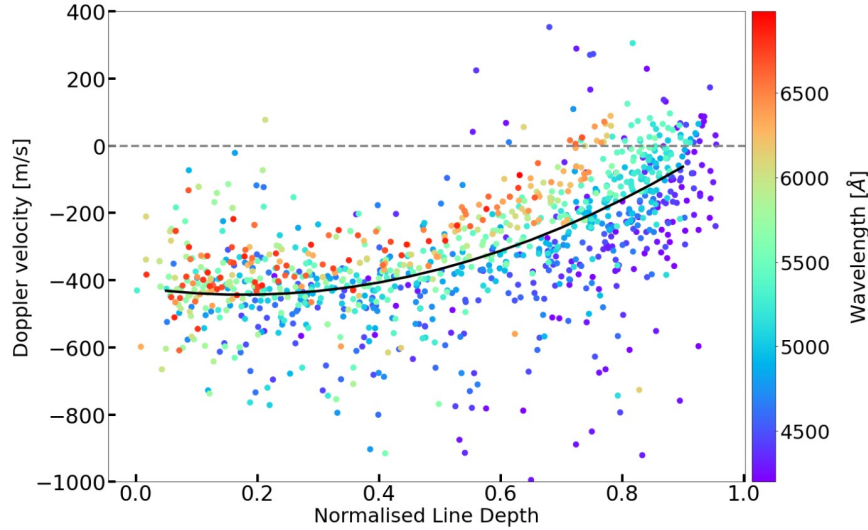


Figure 2.9: Granulation pattern for the IAG spatially resolved quiet sun atlas, is shown to have a strong chromodependence in the weaker lines. Image taken from [6].

effect but as the velocities can be significant, the relativistic formulation of this effect must be applied.

The relativistic Doppler effect accounts for length contraction, as predicted by Einstein's theory of relativity. This introduces an additional correction term to the classical shift, which becomes particularly relevant in high-velocity scenarios or strong gravitational fields. However, the measured negative redshift resulting from convective motions is known as *convective blueshifts* which are measured by the equation (??).

$$v_r \approx c \left( \frac{\lambda_{obs} - \lambda_{rep}}{\lambda_{rep}} \right) \quad (2.7)$$

Since the strength of the convective distortions and shifts as spectral lines varies across the H-R diagram, we expect the systematic errors in radial velocities [7].

#### 2.4.5 Chromodependence characterization

Recently, the emphasis on the measurement of granulation pattern has opened new interpretations to the line depth-dependent wavelength shifts. However, there is still no characterization for this phenomenon.

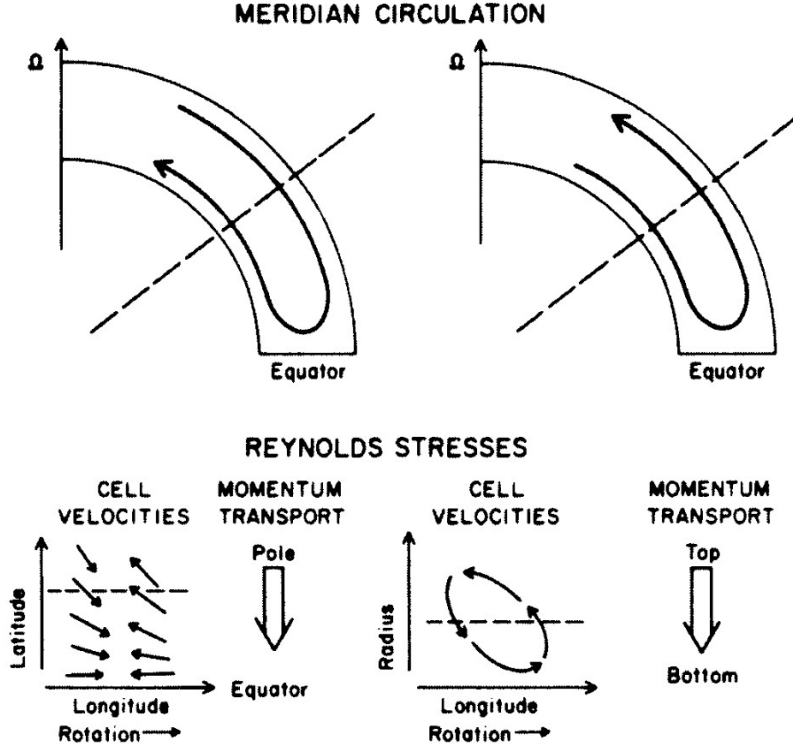


Figure 2.10: Contributions on angular momentum. Image taken from [4].

In 2018 Gray and Oostra try to establish a standard curve determined by the second grade polynomial fit to the solar granulation pattern. Although, the authors just take into account the range of  $4950\text{\AA}$  to  $5700\text{\AA}$  of the spectrum, avoiding the chromodependence in the weaker lines. This motivates to search a strong characterization and give the recipe for dealing with this phenomenon.

Hamilton and Lester, give a little theory that this phenomenon is attributed to the rotation in the photosphere. The pronounced differential rotation with latitude observed at the photosphere seems to be the result of convective flows driven radially by the buoyancy force and deflected horizontally by the coriolis force due to solar rotation [4]. This rotation made contributions on angular momentum in two different forms: Meridian circulation and Reynolds stresses.

The first contribution occurs if axisymmetric meridional circulation are present (see figure 2.10). In the absence of any other angular momentum transport, a circulation in either sense will tend to spin up the poles and the interior because the fluid carries angular momentum.

The second contribution tends to enforce solid body rotation, then the meridional circulation drive an equatorial acceleration. The reason is for equal velocity in the meridional plane, the flux of angular momentum per unit mass across the dashed line will be larger toward the equator than away from it. This mechanism depends on the existence of nonaxisymmetric convective motion because net fluxes of angular momentum in latitudinal or radials directions are produced without requiring a net mass flux. Neither buoyancy forces, which are strictly radial, nor pressure gradients, which must average to zero around the solar circumference, can themselves influences the suns axysimetric rotation profile [4].

# Chapter 3

## Methodology: The blend-free list of Fe I lines

As the spectral analysis is complicated due to convective motion this project takes a computational approach leading to an observational requirement, by the experience of professor Benjamin and previous research. For the computational part, the programming language Python and Jupyter Notebook was used. All analysis data and code used in the process was uploaded to a GitHub repository [17], allowing anyone interested to reproduce the results and verify the authenticity of the conclusions presented. Moreover, proper credit will be given to all previous work from other researchers.

We follow the methodology established in previous studies (see [10] and references therein), which utilized a selected list of Fe I lines. As mentioned before these lines are ideal for this calibration due to their minimal thermal broadening and reduced susceptibility to other atmospheric affectations.

### 3.1 Computational approach

The computational aspect focuses on identifying the granulation pattern within the solar spectrum by calculating relative velocities using the wavelengths of Fe I.

The line up was to identify the Fe I lines in the IAG Solar Flux Atlas and the IAG Spatially

Resolved Quiet Sun Atlas using the blend-free list of Fe I lines. Second, fit a fourth-grade polynomial fit due to the c-curved line profile bisector and find the observed wavelength. For an optimal fit was used a z-score standardization on each line core, which is explained in appendix A. Then calculate the observed wavelength, Doppler velocity and convective blueshift based on the polynomial fit. Finally, find the values for the line core curvature (see equation (2.5)) and the line core bisector slope (see equation (2.6)).

## 3.2 Blend-free Fe I line list

The previous line up implemented the Nave et. al list of laboratory measured Fe I lines [12]. This list classifies lines with a quality rating (A,B,C,D) with A be the most and best quality. However, not all the listed lines are clearly present in the solar spectrum, and within the near-infrared range, many lines are severely mixed.

In collaboration with Professor Benjamin and Manuel Fuentes, we refined this list using different approaches.

### 3.2.1 Selection method for Fe I lines

The process of selection has two different approaches: Computational and visual. First, we selected only quality A lines for the Nave list and then performed statistical filters according to the statement of having a fourth order polynomial fit for the line core.

The filters consist of three general aspects. First, the coefficient of the fourth grade term needs to be positive and not too small because it denotes a wide curve. Specially, this can be for a line in the infrared due the big core curvatures are related to atmospheric lines. Second, the difference between extreme points of the fit needs to be less than half of the distance. This filter helps identify lines which are not slopes and have a core. Finally, the absolute difference between the wavelength observed and the emitted (from Nave list) needs to be less to  $0.025\text{\AA}$ .

### **3.2.2 Observational requirement**

The last part of the selection was a visual inspection to discard line mixes or absent from the solar spectrum. The use of a visualizer application (explained in detail in the appendix C) was useful to see simultaneously the graphic for the line core and the behavior in the line core curvature, line bisector slope and granulation pattern plots. The discard part was using the geometry of the curve, behavior on plots and the guidance of professor Benjamin.

The final part of the methodology was to perform different plots for our analysis. This is based on the requirement for the characterization.

# **Chapter 4**

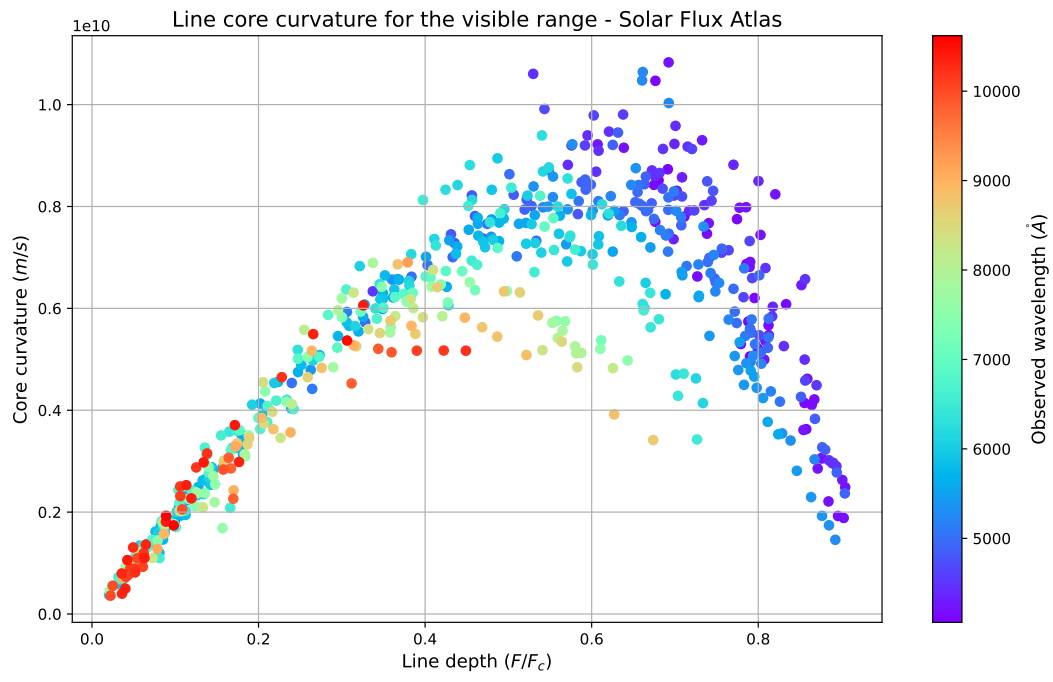
## **Results and discussion: Granulation pattern and Characterization of chromodependence**

Our results can be summarized in three principal aspects: Chromodependence on the granulation pattern along the line depth; a detailed view of the first and second signature; and higher-quality graphs with reduced scatter.

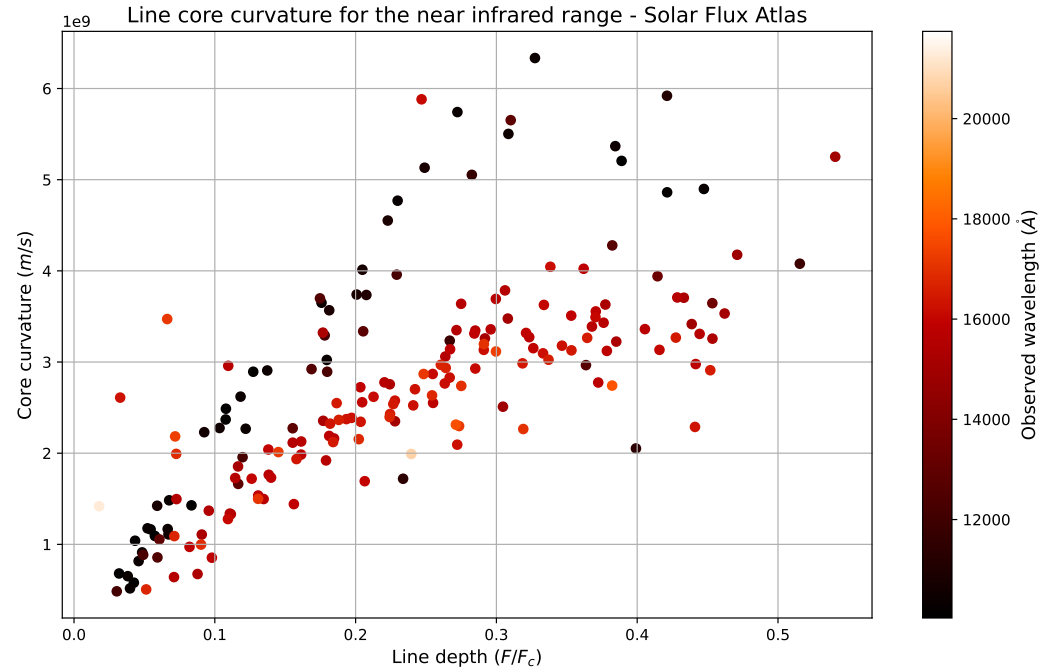
### **4.1 The first signature**

#### **4.1.1 Detailed view of line broadening**

The core curvature was calculated following the equation (2.5) and plotted against line depth as shown in figure 4.1.



(a) Visible range.



(b) Near infrared range.

Figure 4.1: Line core curvature in the Solar Flux Atlas. Is visible a characteristic curve with  
29 line depth-dependence along wavelength.

As shown in the figure 4.1b, the plot for the near infrared range is visible a natural division for wavelengths in  $11400\text{\AA}$ , which corresponds to telluric lines of absorption in the atmosphere. Plotting all ranges of the Solar Flux Atlas is visible a line depth-dependence along wavelength.

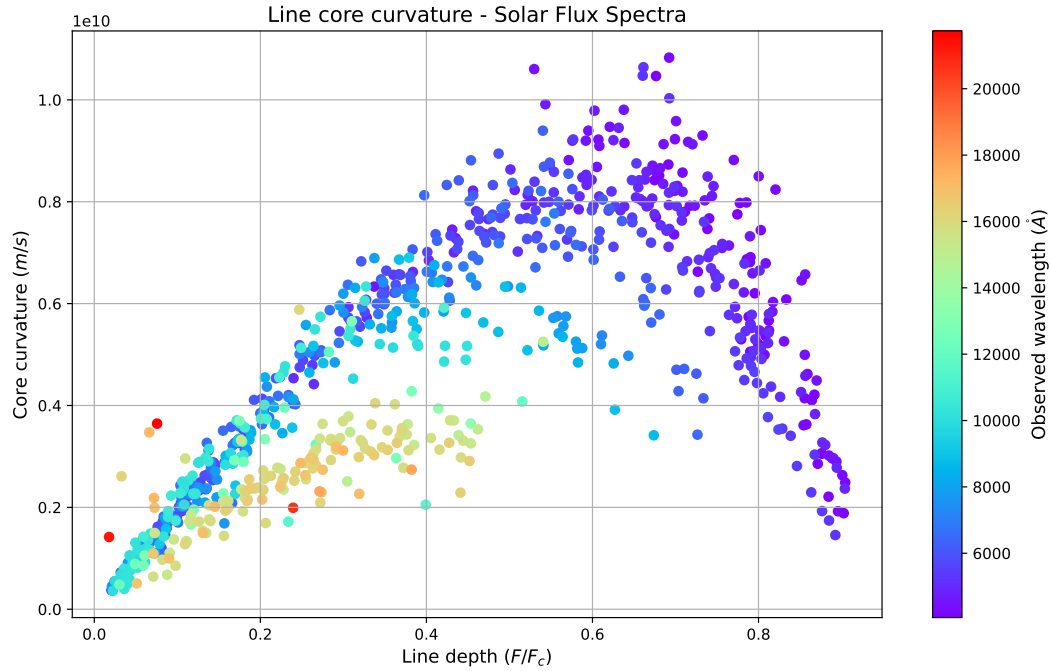


Figure 4.2: Line core curvature in the Solar Flux Atlas. The near infrared range presents a natural division due telluric lines in the atmosphere.

As shown in figure 4.2 the chromodepence presented on the third signature plot is characteristic of weaker lines. This type of lines are known to represent the lower potential excitations.

## 4.2 The second signature

### 4.2.1 Detailed view of line profile bisector asymmetry

The figure 4.3 shows the behavior of the C-curved line profile bisector.

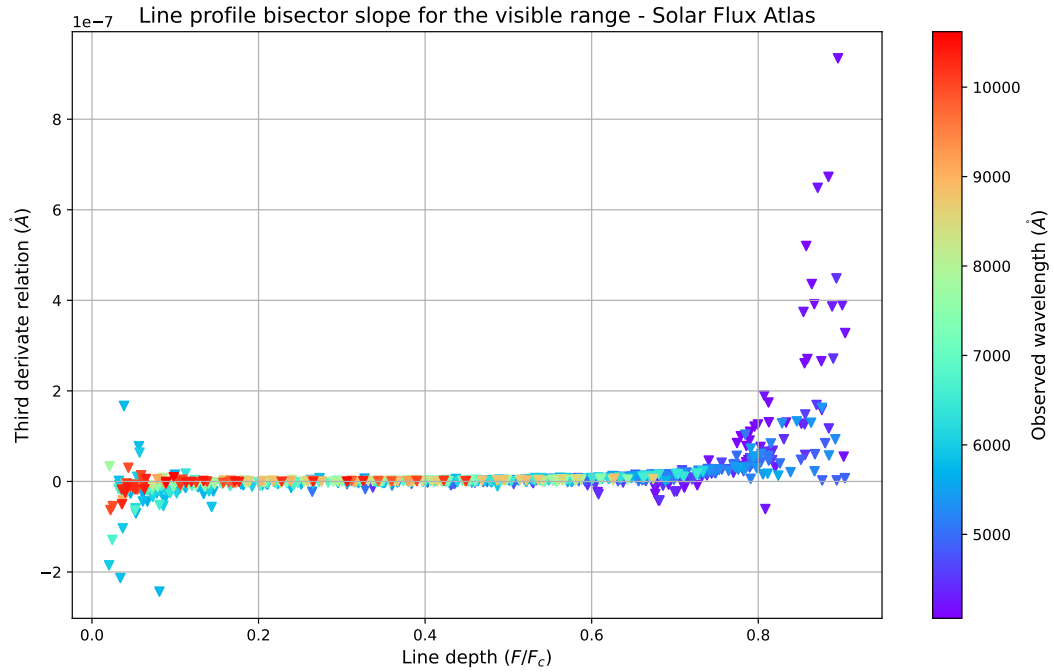


Figure 4.3: Line profile bisector slope for the Solar Flux Atlas separated by wavelength range. The behavior of the plot is according to the C-curved shape of the line bisector affected by convection movement.

The behavior of the plot is according to the C-curved shape of the line bisector affected by convection movement, and calculated following the equation (2.6).

## 4.3 The third signature

### 4.3.1 Chromodependence on the granulation pattern

The granulation patterns for the IAG Solar Flux Atlas in all the wavelength range was obtained.

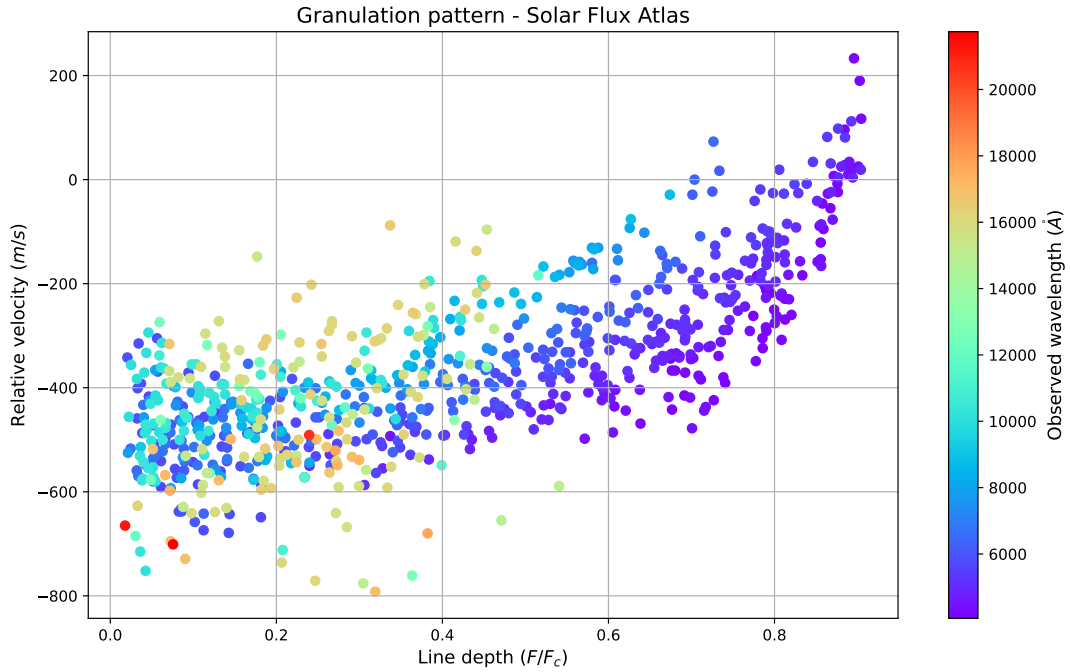


Figure 4.4: Granulation pattern obtained for the Solar Flux Atlas. The wavelength shift dependence is along the line depth.

As shown in the figure 4.4 the behavior along the line depth is according to literature, in which is clear the wavelength shift dependence along the line depth or chromodependence.

### 4.3.2 Characterization of chromodepence on granulation pattern

As mentioned before, the characterization given to this plot by Gray and Oostra [14] don't take into account all the wavelengths.

For a different perspective into the characterization of this behavior, different second order polynomials fit for each color range were generated.

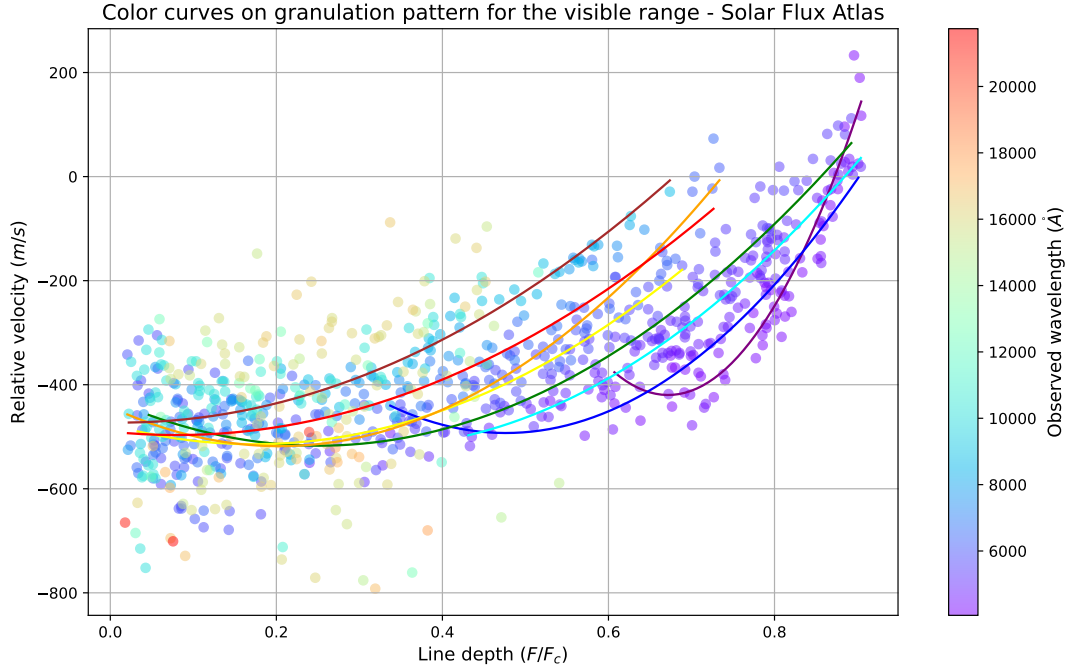


Figure 4.5: Granulation pattern for the Solar Flux Atlas with color curves. The tendency on the curves is more pronounced in the violet and red range.

The tendency on the curves is more pronounced in the violet and red range. This can be interpreted as the standard curve from Gray and Oostra is shifted and flattened along decreasing wavelengths. The coefficients of each color curve were plotted in figure 4.6.

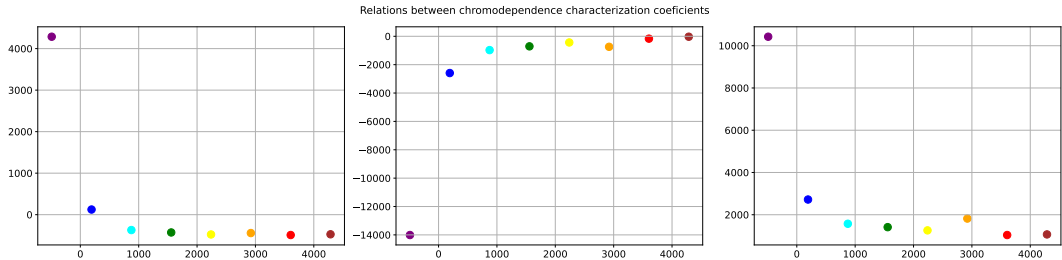


Figure 4.6: Coefficient tendency for the second order polynomial fit in each color curve. All of the coefficients show a rational increment with decreasing wavelength.

All of the coefficients show a rational increment with decreasing wavelength, the values are

shown in the table 4.1.

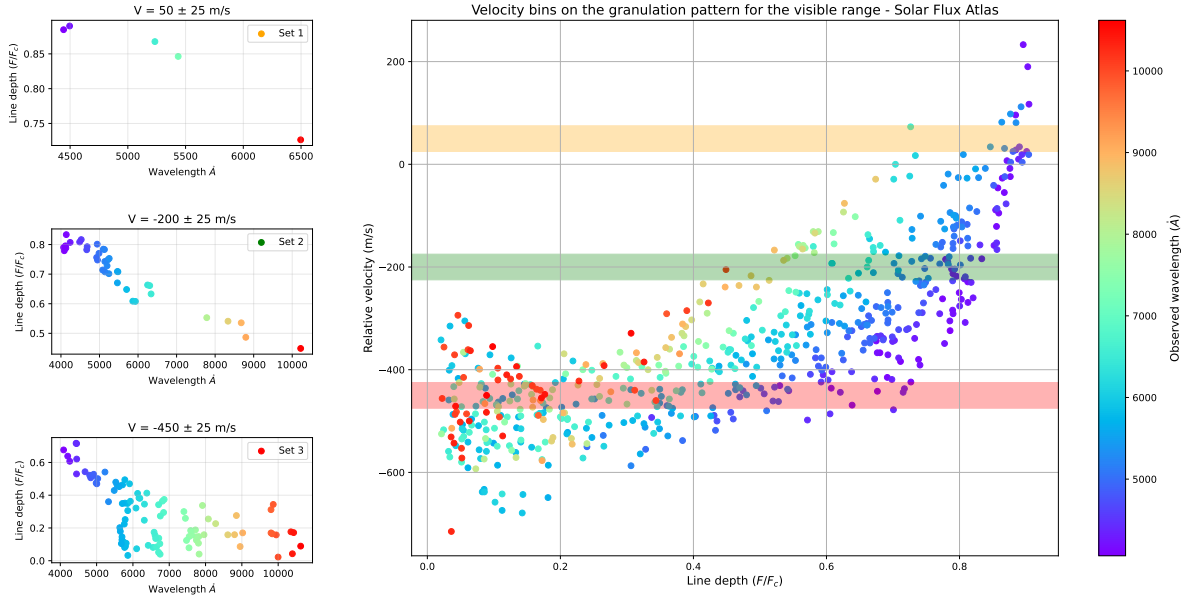
Wavelength range ( $\text{\AA}$ )	Second order	First order	Shift
3800-4270	4924.2052	-14022.7063	10434.9782
4270-4760	757.0966	-2590.7356	2719.8840
4760-4970	263.3435	-974.5109	1574.3597
4970-5700	204.8798	-709.6070	1413.5460
5700-5810	155.9806	-432.9495	1256.0760
5810-6180	190.1927	-739.9248	1818.1626
6180-7800	142.9648	-166.1503	1039.8561
7800-11000	160.4951	-29.5577	1067.7370

Table 4.1: Values for the coefficients shown in figure 4.6

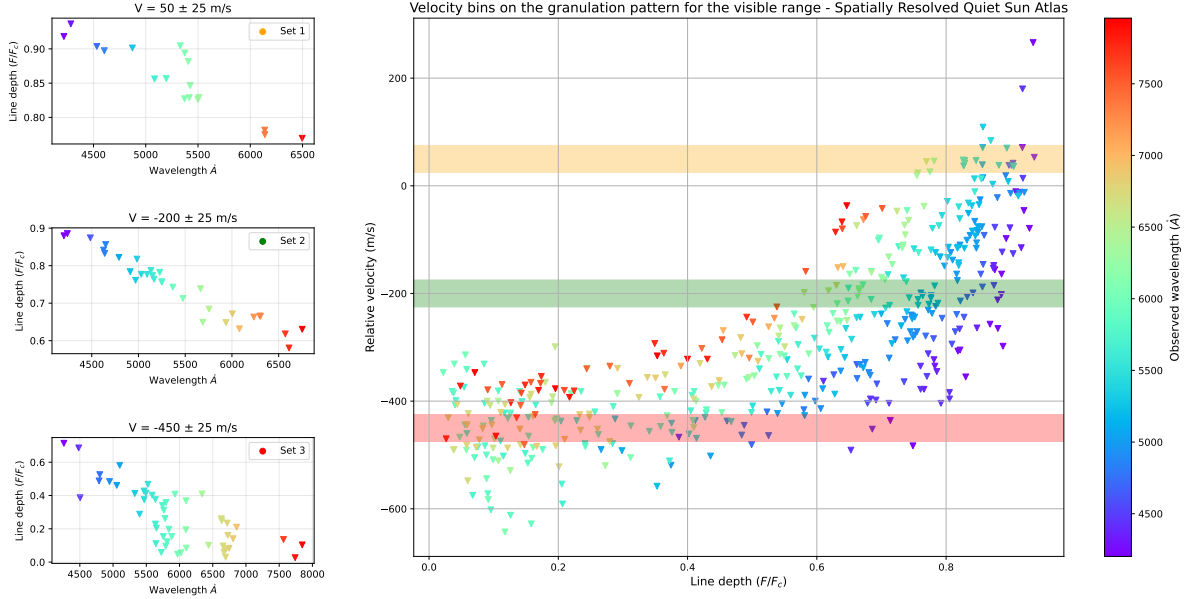
### 4.3.3 Frequency shifts for rotation hypothesis

For a description of this tendency was performed an analysis of line depth against wavelength. The hypothesis was: “If there exists a frequency shift only in the Solar Flux Atlas, then rotation could be the cause of this phenomenon.” However, the frequency shift was observed in both spectral datasets. This was initially unexpected because the rotation is negligible at the disc center.

For the measurement of its frequency, a range from  $4300\text{\AA}$  to  $5600\text{\AA}$  was taken. Then was sorted all wavelengths from both atlases into 50 m/s velocity bins (see figure ??).



(a) Visible range for the Solar Flux Atlas.

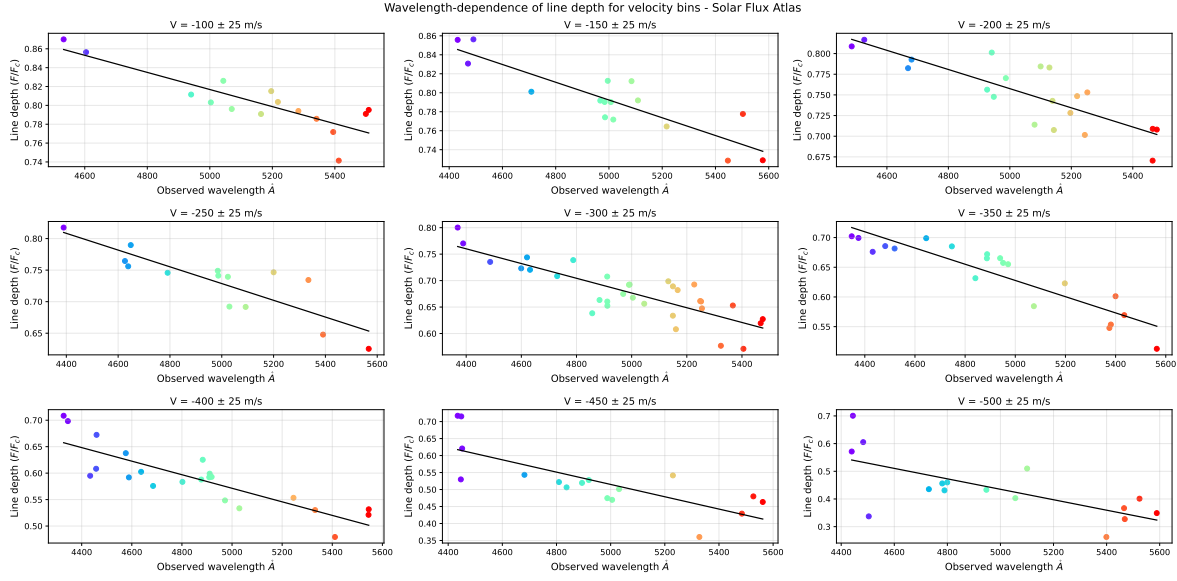


(b) Visible range for the Spatially Resolved Quiet Sun Atlas.

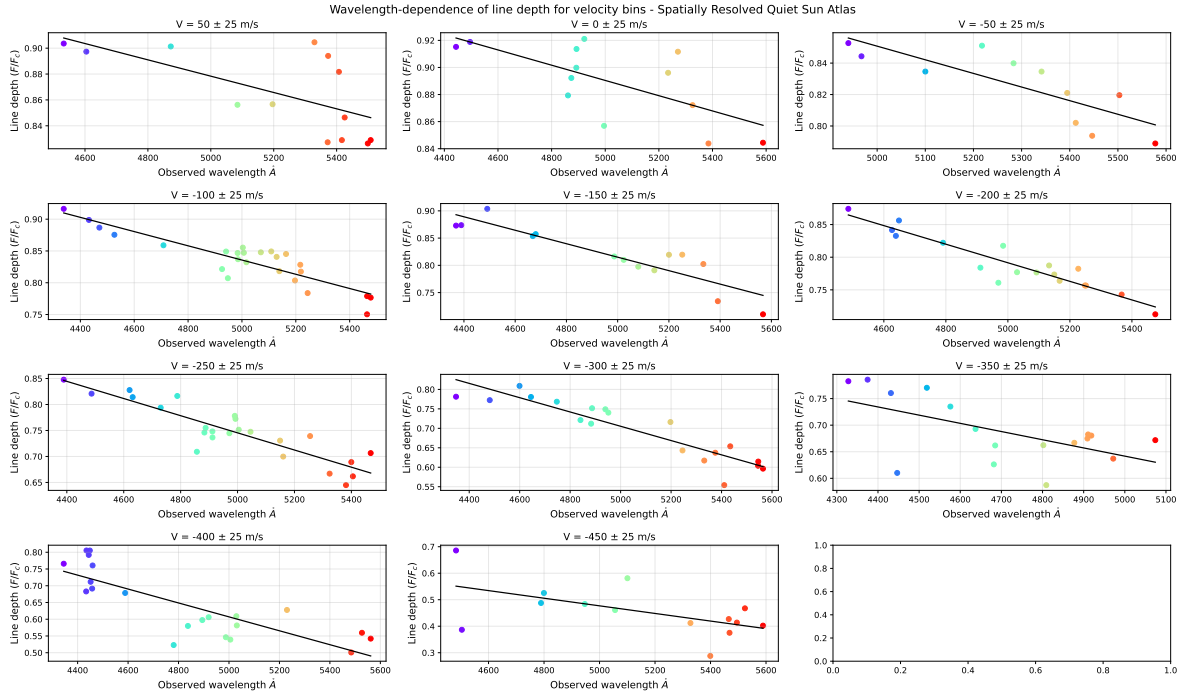
Figure 4.7: Comparision between atlases with velocity bins for the relation between wavelength and line depth. For each velocity bin was plotted wavelength against line depth to measure a frequency shift with a first order polynomial fit.

For each velocity bin was plotted wavelength against line depth to measure a frequency shift

with a first order polynomial fit (see figure 4.8)



(a) Velocity bins for the Solar Flux Atlas plot (see figure 4.7a).



(b) Velocity bins for the Spatially Resolved Quiet Sun Atlas (see figure 4.7b).

Figure 4.8: Comparision between atlases with velocity bins for the relation between wavelength and line depth. The first order fit is showed for each velocity bin.

The table ?? shows the obtained slopes in both atlases. The value of slopes for the Spatially Resolved Quiet Sun Atlas are greater than the Solar Flux Atlas, which contradicts the initial hypothesis. There is no existence of frequency shifts in the granulation patterns.

## 4.4 Higher quality graphs

To show the improvement on the quality in the third signature plots, the figure 4.9 compare the plot obtained by Ellwarth [6] and the graphic.

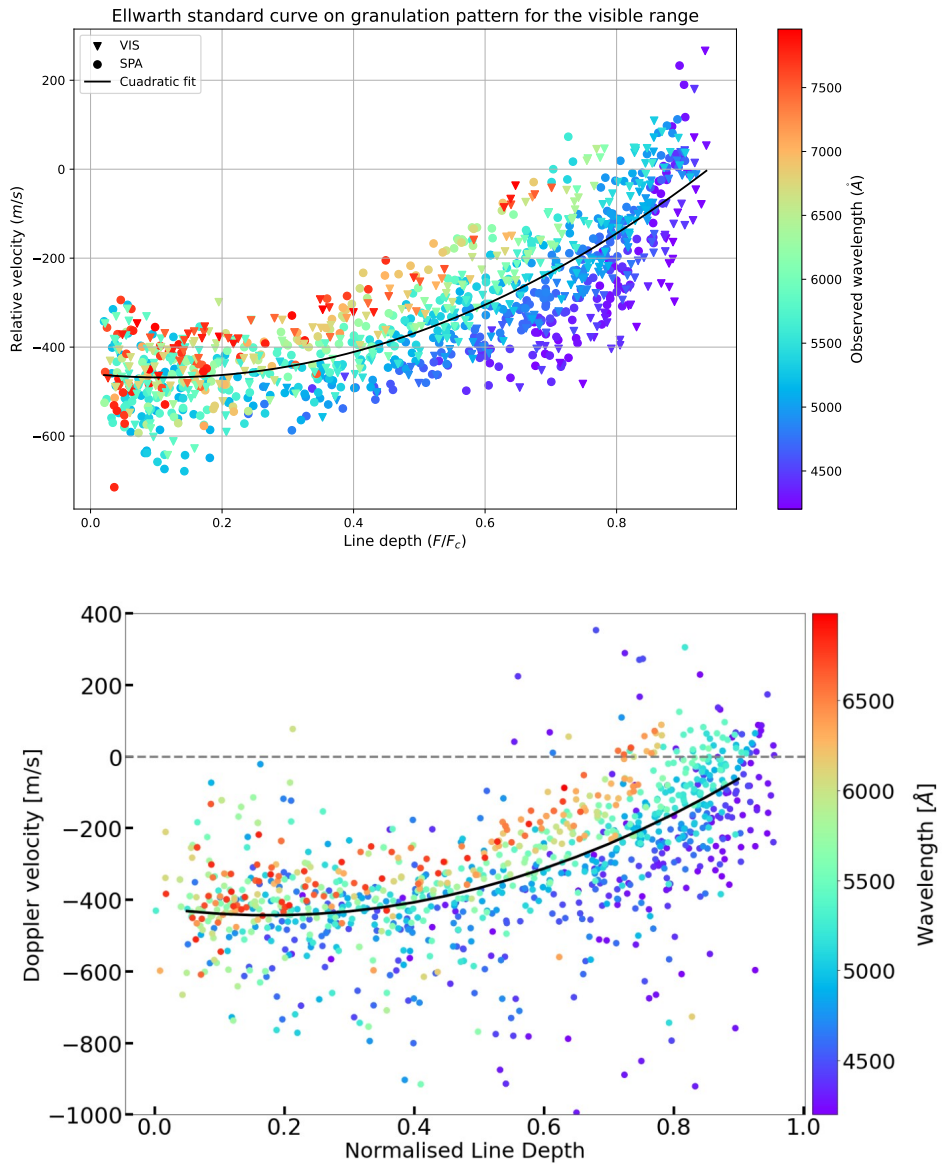


Figure 4.9: We realized the same graphic for the comparision with the Ellwarth article to show the less scattered points.

The less scattered points and the improvement on the chromodepence identification is evident.

# Chapter 5

## Conclusions

In general, we conclude... Characterize the convective blueshift of solar absorption lines and its dependence on line depth and wavelength range.

In specific, we produce a blend-free list of Fe I absorption lines and solar granulation patterns with minimal scatter. We describe in detail how the granulation plot depends on wavelength range. We explore possible explanations of wavelength-dependence and found thats () is the best. We explore ways of dealing with the wavelength-dependence when using the solar spectrum as a gauge for stellar spectra.

# Appendix A

## Z-score Standardization

In the process of calculate the four order polynomial fit the function `np.polyfit()` presents an overestimation on the coefficients, due to the large difference of magnitude order between axis. To deal with this difference a z-score standardization was used on the selected bins of wavelengths around the observed wavelength. This process helps to avoid the dominance of certain features over other due to differences in their scales [18].

The follow up for the standardization was applied the relation (A.1) on the selected bins for wavelength.

$$\lambda_{scaled} = \frac{\lambda - \mu(\lambda)}{\sigma(\lambda)} \quad (\text{A.1})$$

Where  $\mu(\lambda)$  refers to the mean and  $\sigma(\lambda)$  to the standard deviation of the wavelength range. As the wavelength was scaled, in terms of calculated derivates for the first and the second signature, a re-scaled for this values was necessary. Based on the definition for the standardization, the derivates follow the relation (A.2).

$$\frac{d}{d\lambda} = \frac{1}{\sigma(\lambda)} \frac{d}{d\lambda_{scaled}} \quad (\text{A.2})$$

Taking the derivate of the expresion (A.1) a factor related to the standard deviation appear. With this, the original values for derivates evaluated in the observed wavelength are expresed in equation (A.3)

$$\frac{d^2}{d\lambda^2} = \frac{1}{\sigma(\lambda)^2} \frac{d^2}{d\lambda_{scaled}^2} \quad \quad \frac{d^3}{d\lambda^3} = \frac{1}{\sigma(\lambda)^3} \frac{d^3}{d\lambda_{scaled}^3} \quad \quad \text{(A.3)}$$

This improved considerably the precision in the fit and there over the precision on the observed wavelength calculated.

# **Appendix B**

## **The third derivate relation**

Or called the bisector slope. It was multiplied by the relation  $(\frac{c}{\lambda})$  to see each clear in the graphic.

# **Appendix C**

## **Visualizer for outliers**

For the process of the blend-free list was created an app using the interface Tkinter with the objective for help the visualization of outliers. Two version of the visualizer were created. One just show the line core and forthh order polynomial fit as shown in the figure () .

This helps for a first process where far separated lines were discarded. Then, we can perform the different calculations and use the second version of the visualizer (see figure () ).

In this version the vision of the thre signature of conevction and the line core with the fit. Moreover, was resalted the correspond Fe I line on each graph to corroborated the behavior. Thanks to this the time expended seeing lines was reduced signfically.

# Bibliography

- [1] P. Eric, *Solar magnetohydrodynamics*. Kluwer, 1982.
- [2] J.-M. Malherbe, “Jules janssen, the birth of solar physics, the foundation of meudon observatory and the mont blanc adventure (1875-1895),” *HAL CNRS*, Aug. 2022.
- [3] S. A. Hamouda, F. F. Alfarjani, and F. Y. Elfituri, “Sunspots production and relation to other phenomena: A review,” *International Journal of Science and Research Methodology*, 06 2018.
- [4] F. Peter, *Solar Astrophysics*. Cambridge research and instrumentation, 1990.
- [5] T. A. Nieminen, “Solar line asymmetries: Modelling the effect of granulation on the solar spectrum,” *arXiv*, Aug. 2017. arXiv:1708.06408 [astro-ph].
- [6] M. Ellwarth, B. Ehmann, S. Schäfer, and A. Reiners, “Convective characteristics of fe i lines across the solar disc,” *Astronomy and Astrophysics*, vol. 680, p. A62, Dec. 2023.
- [7] D. F. Gray, “The third signature of stellar granulation,” *The Astrophysical Journal*, vol. 697, p. 1032, May 2009.
- [8] D. Hamilton and J. B. Lester, “A technique for the study of stellar convection: The visible solar flux spectrum,” *Publications of the Astronomical Society of the Pacific*, vol. 111, p. 1132, Sept. 1999.
- [9] A. Reiners, N. Mrotzek, U. Lemke, J. Hinrichs, and K. Reinsch, “The iag solar flux atlas: Accurate wavelengths and absolute convective blueshift in standard solar spectra,” *Astronomy and Astrophysics*, vol. 587, p. A65, Mar. 2016.

- [10] D. Dravins, L. Lindegren, and A. Nordlund, “Solar granulation - influence of convection on spectral line asymmetries and wavelength shifts,” *Astronomy and Astrophysics*, vol. 96, p. 345–364, Mar. 1981.
- [11] D. F. Gray and T. Pugh, “The third signature of granulation in bright-giant and supergiant stars,” *The Astronomical Journal*, vol. 143, p. 92, Mar. 2012.
- [12] G. Nave, S. Johansson, R. C. M. Learner, A. P. Thorne, and J. W. Brault, “A new multiplet table for fe i,” *The Astrophysical Journal Supplement Series*, vol. 94, p. 221, Sept. 1994.
- [13] A. Cacciani, R. Briguglio, F. Massa, and P. Rapex, “Precise measurement of the solar gravitational red shift,” *Celestial Mechanics and Dynamical Astronomy*, vol. 95, p. 425–437, May 2006.
- [14] D. F. Gray and B. Oostra, “The solar-flux third granulation signature,” *The Astrophysical Journal*, vol. 852, p. 42, Jan. 2018. ADS Bibcode: 2018ApJ...852...42G.
- [15] H. H. Plaskett, “Solar granulation,” *Monthly Notices of the Royal Astronomical Society*, vol. 96, p. 402, Mar. 1936. ADS Bibcode: 1936MNRAS..96..402P.
- [16] B. Carroll and D. Ostlie, *An Introduction to Modern Astrophysics*. Cambridge University Press, 2017.
- [17] C. Cuellar, “Final project.” online, 2025.
- [18] J. P. Boyd, *Solving Transcendental Equations: The Chebyshev Polynomial Proxy and Other Numerical Rootfinders, Perturbation Series, and Oracles*. SIAM, Oct. 2014. Google-Books-ID: ANGgBAAAQBAJ.
- [19] J. S. Aponte, *Medición de la velocidad convectiva en la fotosfera solar*. Bachelor’s thesis, Universidad de los Andes, 2017.
- [20] F. Stief, J. Löhner-Böttcher, W. Schmidt, T. Steinmetz, and R. Holzwarth, “Convective blueshifts in the solar atmosphere - ii. high-accuracy observations of the fe i 6173.3 Å line

and deviations of full-disk dopplergrams,” *Astronomy & Astrophysics*, vol. 622, p. A34, Feb. 2019.